USGS Award Number G11AP20014

Broadband Seismograms from Dynamic Ruptures on Rough Faults: Validation Against Strong Motion Data

Eric M. Dunham

Department of Geophysics, Stanford University
397 Panama Mall
Stanford, CA 94305
tel: (650) 725-6989, fax: (650) 725-7344, email: edunham@stanford.edu

Term: 12/10/2010 through 06/09/2012

Abstract: Strong ground motion records have a random character at frequencies above ~1 Hz. The origin of this complexity is poorly understood, despite the engineering importance of ~1-10 Hz shaking. Possible explanations include source complexity and scattering of seismic waves along their propagation paths. In this project, we used dynamic rupture models to explore the first possibility. We studied how geometric complexity of the fault surface alters rupture propagation, leading to accelerations and decelerations of the rupture front in response to local slip-induced stress heterogeneity. These rupture velocity fluctuations, together with short-wavelength slip variability and changes in the local fault orientation, destroy coherence of the radiated seismic wavefield at sufficiently high frequencies. We identified and quantified this effect by generating synthetic far-field body wave seismograms from our dynamic rupture models. Plots of the Fourier spectral amplitude over narrow frequency ranges show a transition from a double couple radiation pattern with pronounced directivity at low frequencies to a more isotropic pattern at high frequencies. Directivity effects diminish at high frequencies for P waves, but not S waves, as a result of source complexity. These numerical calculations inspired development of an analytical model, based on the seismic representation theorem, which accounts for the leading order effects of fault nonplanarity on far-field radiation. For S waves, for example, the usual radiation pattern is proportional to $\cos(2\theta)$; the correction term from fault roughness is proportional to $\sin(2\theta)$, thereby filling in the nodes of the radiation pattern. In addition to this theoretical and modeling work, we also began efforts to validate our theoretical predictions against strong motion data. We focused on the extremely well recorded Mw 6.6 2000 Tottori, Japan, earthquake. We processed many hundred K-net and KiK-net strong motion records to obtain root mean square acceleration within different frequency bands as a function of distance and azimuth. The next step is to perform least squares fits to our model predictions. After validation, our simple analytical expressions can then be used in kinematic rupture models to efficiently generate synthetic broadband seismograms.

Report: This project focused on the generation of synthetic broadband seismograms and comparison with data. Existing deterministic simulations methods, either kinematic or dynamic, are quite successful at reproducing key features of strong motion records at frequencies below ∼1 Hz. However, due to lack of knowledge about the earthquake source and heterogeneities of the medium at scales below ∼1 km, it is quite challenging to accurately simulate high frequency ground motion above ∼1 Hz. This project focused specifically on the role of earthquake source complexity in generating high frequency ground motion.

Motivated by recent high-resolution measurements of fault surface roughness, we conducted dynamic rupture models on bandlimited self-similar fractal faults (Figure 1). The models were two-dimensional plane strain, with roughness included at scales greater than ∼100 m on faults extending ∼100 km. We used strongly velocity-weakening friction laws in a rate-and-state framework, consistent with high-velocity laboratory experiments. We also accounted for off-fault plasticity. We ran several hundred simulations, each with different realizations of the random fault geometry, as well as different prestress conditions and amplitude-to-wavelength ratio of roughness.

For each simulation, we used the seismic representation theorem to calculate far-field ground motion, both in the time and frequency domains (Figure 2). It is only in the far-field limit that there are well-defined radiation patterns, and this is where we see the most potential for quantifying these effects and comparing to observations.

The far-field body wave displacement spectrum can be written as

$$\begin{aligned} \hat{u}_i(r_0, \phi, \omega) &= \frac{R_{ijk}}{4\pi\rho c^3 r_0} e^{i\omega r_0/c} \int \mu W \hat{V}(x', \omega) e^{-i\omega x' \cos\phi/c} \\ &\quad [n_j(x') s_k(x') + n_k(x') s_j(x')]\, dx', \end{aligned} \tag{1}$$

where r_0 is the distance from the hypocenter to the station, ϕ is the azimuthal angle, $\omega = 2\pi f$ is the angular frequency, R_{ijk} is the radiation pattern tensor, μ is shear modulus, ρ is density, and c is the wave speed. The fault width is W and we have focused on waves with wavelengths larger than the fault width in writing the above expression. The integral is over the fault curve and we have neglected the second-order correction to the differential arc length. The Fourier transform of the slip velocity $V(x,t)$ is

$$\hat{V}(x, \omega) = \int_{-\infty}^{\infty} V(x,t) e^{i\omega t} dt. \tag{2}$$

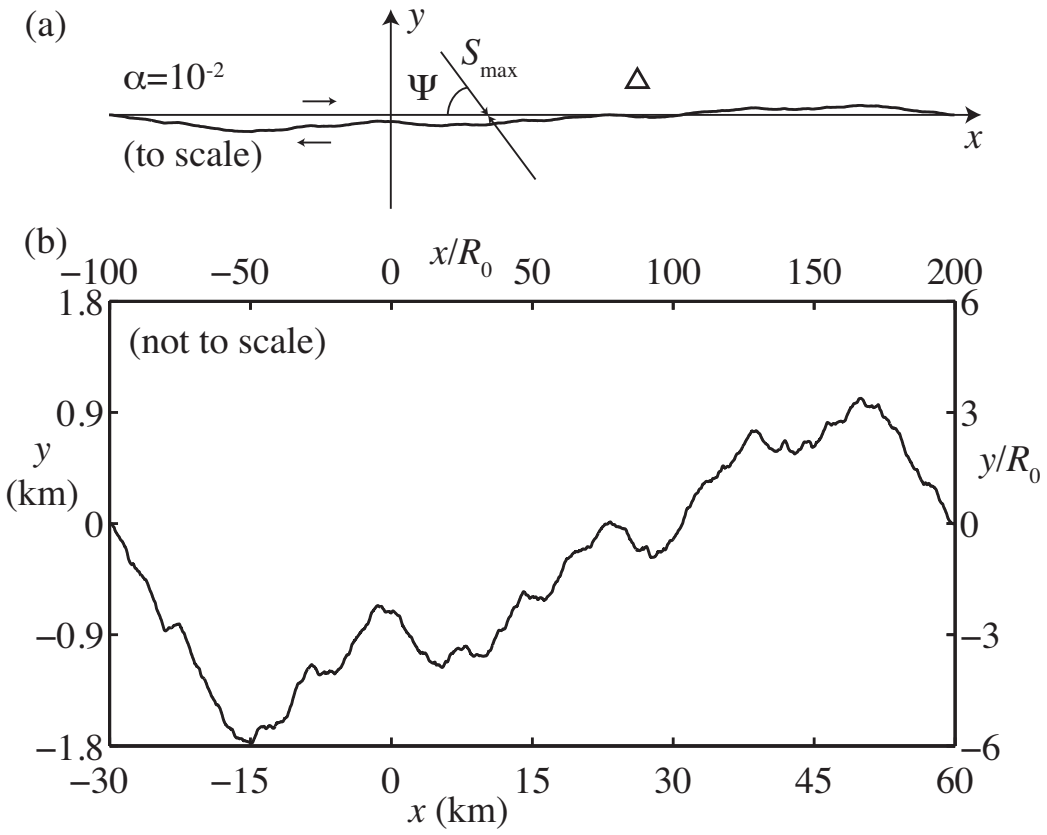

Figure 1: Bandlimited self-similar fault profile, $y = h(x)$, with amplitude-to-wavelength ratio $\alpha = 10^{-2}$, shown (a) to scale, and (b) exaggerated in the y-direction to emphasize fluctuations. The maximum principal stress, $S_{\max}$, is inclined at angle Ψ to $y = 0$.

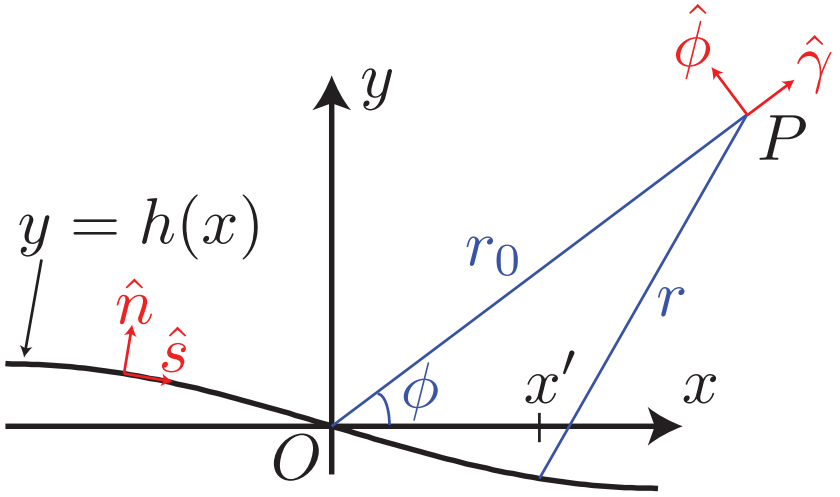

Figure 2: Far-field radiation from rupture on a nonplanar fault $y = h(x)$. The unit normal and tangent vectors are $\hat{n}$ and $\hat{s}$, respectively. The seismic signal observed at point P is obtained by integrating contributions from all parts of the fault. The waves from the point $(x', h(x'))$ travel the distance $r \approx r_0 - x' \cos\phi$, where r_0 is the distance from the origin O (located on the fault) to the far-field station P and ϕ is the azimuthal angle. We have neglected the small correction to the travel distance from fault nonplanarity in this approximation. Both r_0 and ϕ are constant for a given observation point P and are independent of the specific fault patch under consideration. P and S waves arriving at P will be polarized in the radial ($\hat{\gamma}$) and transverse ($\hat{\phi}$) directions.

The P- and S-wave radiation pattern and polarization tensors are

$$R^p_{ijk} = \gamma_i\gamma_j\gamma_k \quad \text{and} \quad R^s_{ijk} = (1/2)(\delta_{ij}\gamma_k + \delta_{ik}\gamma_j) - \gamma_i\gamma_j\gamma_k. \tag{3}$$

P- and S-waves from a small fault patch at $(x, h(x))$ are proportional to the amplitude factors

$$\begin{aligned} A^p(x) &= \gamma_i R^p_{ijk}\,[n_j(x)s_k(x) + n_k(x)s_j(x)] \\ &= \gamma_j\gamma_k(n_j s_k + n_k s_j) \\ &= 2(\hat{\gamma}\cdot\hat{n})(\hat{\gamma}\cdot\hat{s}) \end{aligned} \tag{4}$$

and

$$A^s(x) = \hat{\phi}_i R^s_{ijk}\,[n_j(x)s_k(x) + n_k(x)s_j(x)]$$

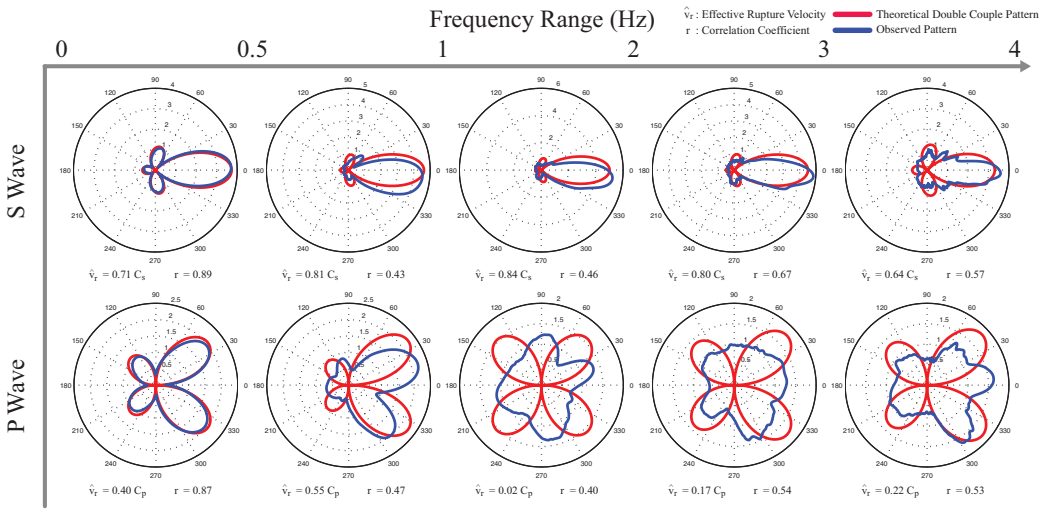

Figure 3: Radiation patterns from a spontaneous rupture on a rough fault, shown for P and S waves (bottom and top rows, respectively) as a function of frequency (averaged over frequency bins 0–0.5 Hz, 0.5–1 Hz, etc.). Blue lines show radiation patterns from simulations; red lines are best-fitting double couple pattern with directivity. Shown below each subplot is the effective rupture velocity $\hat{v}_r$ that determines the degree of directivity and the correlation coefficient r that quantifies the quality of the fit.

$$\begin{aligned} &= (1/2)(\hat{\phi}_j\gamma_k + \hat{\phi}_k\gamma_j)(n_j s_k + n_k s_j) \\ &= (\hat{\phi}\cdot\hat{n})(\hat{\gamma}\cdot\hat{s}) + (\hat{\phi}\cdot\hat{s})(\hat{\gamma}\cdot\hat{n}). \end{aligned} \tag{5}$$

We used these formulas to calculate far-field ground motion. One of our key results is shown in Figure 3. We find that radiation patterns evolve as a function of frequency, from a clear double couple with directivity at low frequencies to a more isotropic radiation pattern at high frequencies. Directivity effects are lost at high frequencies for P waves, but not S waves. The transition to isotropy occurs around ∼1 Hz, consistent with observations.

To better understand why this happens, we turned to the representation theorem. Define $m(x) = h'(x)$ as the fault slope. For small slope, approximate $\hat{n}$ and $\hat{s}$ to first order:

$$\hat{\gamma}\cdot\hat{n} = -m\cos\phi + \sin\phi, \tag{6}$$

$$\hat{\gamma}\cdot\hat{s} = \cos\phi + m\sin\phi, \tag{7}$$

$$\hat{\phi}\cdot\hat{n} = m\sin\phi + \cos\phi, \tag{8}$$

$$\hat{\phi} \cdot \hat{n} \quad = \quad -\sin\phi + m\cos\phi. \tag{9}$$

Using approximations (6)–(9) in (4) and (5) gives

$$A^p(x) \quad = \quad \sin(2\phi) - 2m(x)\cos(2\phi), \tag{10}$$
$$A^s(x) \quad = \quad \cos(2\phi) + 2m(x)\sin(2\phi). \tag{11}$$

These expressions illustrate that nonplanarity introduce simple corrections to the P- and S-wave radiation patterns that are complementary to the usual double-couple radiation pattern. These corrections fill in nodes in the double-couple radiation pattern, and explain the results shown in Figure 3.

We further developed this theory for self-similar fractal faults. We specified the rupture process kinematically using a simple Haskell model of constant rupture velocity v_r and constant slip Δu, but on a nonplanar fault. We were able to directly relate statistical properties of high frequency ground motion to those of the fault profile. One important result is that, in addition to the usual ground motion described by the Haskell model on a flat fault, there are high frequency oscillations from S waves characterized by root-mean-square acceleration given by

$$a_{rms} = \alpha \frac{\mu \Delta u W D v_r}{\sqrt{2}\rho c_s^3 r_0} \omega_{\max}^2 \sin(2\phi), \tag{12}$$

in which $\omega_{\max}$ is the maximum angular frequency of the ground motion record and

$$D = \frac{1}{1 - (v_r/c_s)\cos\phi} \tag{13}$$

is the usual directivity function with c_s being the S-wave speed. This effect vanishes when the fault is flat (amplitude-to-wavelength ratio of roughness $\alpha = 0$) and has a azimuth dependence that is complementary to the usual $\cos(2\theta)$ dependence of far-field S waves.

The ω^2 behavior is not the observed flat acceleration spectrum at high frequencies. There are several effects that we have neglected which would further reduce high frequency coherence. In the above derivation, we assumed S-wave wavelengths exceeding the fault width; at shorter wavelengths, additional destructive interference would reduce the predicted high frequency spectrum from ω^2 to ω. We have also assumed instantaneous slip at the rupture front (i.e., delta function slip velocity history), so convolving with a smoother source time function would again diminish the spectrum at high

frequencies. We are in the process of including these effects in our model. Additional effects that should be incorporated are spatial variability of slip and rupture velocity. Despite the obvious idealizations of our current model, it does offer the first quantification of the role of nonplanarity in altering high frequency ground motion.

Finally, we have begun an effort to validate our model predictions against strong motion data. We have initially focused on the extremely well recorded M_w 6.6 Tottori earthquake (Figure 4). The double couple pattern is evident at low frequencies, but vanishes at high frequencies.

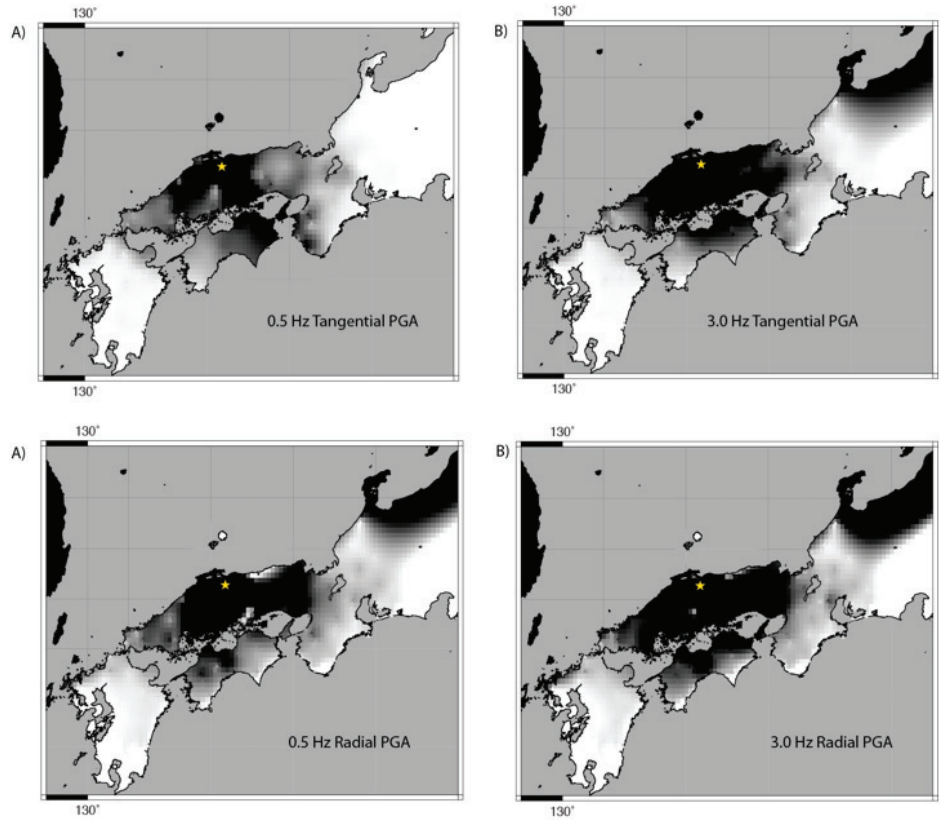

Figure 4: Frequency-dependent radiation patterns observed in the M_w 6.6 Tottori earthquake. This strike-slip has a fault plane striking southeast. (top) PGA for S waves; (bottom) PGA for P waves. (left) Low frequencies around 0.5 Hz; (right) high frequencies around 3 Hz. Similar results are obtained for rms acceleration instead of PGA.

Bibliography (Publications Supported by this Project):

Cho, H., Z. Fang, and E. M. Dunham (2012) Frequency-dependent radiation patterns and directivity effects from earthquake ruptures on nonplanar faults, Bull. Seismol. Soc. Am., in preparation.

Fang, Z., and E. M. Dunham (2012) Additional shear resistance from fault roughness and its role in determining stress levels on mature and immature faults, J. Geophys. Res., in preparation.